Journal of Manufacturing Processes 94 (2023) 564–577

Contents lists available at ScienceDirect

Journal of Manufacturing Processes

journal homepage: www.elsevier.com/locate/manpro

On the possibility of doing reduced order, thermo-fluid modelling of laser powder bed fusion (L-PBF) – Assessment of the importance of recoil pressure and surface tension

W.E. Alphonso [a], M. Baier [b], S. Carmignato [b], J.H. Hattel [a], M. Bayat [a,*]

[a] Department of Mechanical Engineering, Technical University of Denmark (DTU), Kgs. 2800 Lyngby, Denmark
[b] Dept of Management and Engineering, University of Padova, Padova, Italy

ARTICLE INFO

Keywords:
Metal additive manufacturing
L-PBF
Thermal process modelling
Multi-physics simulation
Meso-scale
Stainless steel 316-L

ABSTRACT

Meso-scale, multi-physics simulations of metal additive manufacturing (MAM) processes have so far proven their capability as a reliable tool for predicting potential defect formations. Nevertheless, there is a large number of uncertainty contributions involved with the input process parameters as well as the implemented material properties in these models. As expected, both the process-related and material-related uncertainties affect the outcome of these multi-physics simulations to a large degree. The present work is therefore intended to quantify the impacts of some of the important material/process-related uncertainties involved with meso-scale multi-physics models, on the heat transfer conditions within melt pool. In this respect, a meso-scale multi-physics model of the laser powder bed fusion process of stainless steel 316-L is developed in the commercial Finite Volume Method (FVM) based software Flow-3D and then validated against in-house experiments prior to the main investigation. In the first part of the study, the impact of recoil pressure at different laser linear energy densities (LED) and different laser beam sizes on the melt pool morphology are investigated. It is found that there is a specific threshold of LED below which the melt pool shape is not affected by the recoil pressure and the melt pool fluid dynamics is mostly governed by the Marangoni effect. This threshold increases from 80 J/mm to 280 J/mm when the beam size is increased from 20 μm to 120 μm. Moreover, a parametric study using dimensionless numbers is carried out to understand the impact of different capillary forces on the melt pool shape and size. It is observed that for inverse Bond numbers below $4{\cdot}10^5$, the depth-to-width ratio of the melt pool is above 1 where the recoil pressure dominates the melt pool dynamics and a keyhole forms. In summary, this study specifies in essence the process window over which specific physics are unimportant so that a lower-fidelity meso-scale model could replace the higher-fidelity multi-physics models.

1. Introduction

Additive Manufacturing (AM) also known as 3D printing or Rapid prototyping is a type of advanced manufacturing process that can produce parts from micro to macro scales. AM is classified into the seven groups of material extrusion, material jetting, powder bed fusion, binder jetting (BJ), material jetting, vat photo-polymerization and sheet lamination, according to ISO/ASTM 52900:2021 [1]. The mainstream MAM processes are laser powder bed fusion (L-PBF), electron-beam powder bed fusion (EB-PBF) and direct energy deposition (DED). L-PBF is a branch of MAM in which lasers are used as heating sources for fusing the material together [2]. L-PBF offers many advantages such as reduction in lead times, material waste, high geometric complexity, weight reduction and consolidation of assembly and as such it is becoming highly applicable in aerospace, automotive and bio-medical fields [3]. In addition, as L-PBF locally melts the powder bed the process parameters can be altered to tailor the mechanical and geometrical properties at certain locations hence improving the process efficiency and product quality [2].

In the L-PBF process, a laser is used as heat source and gas-atomized/plasma-atomized powder particles are used as raw material. The basic working principle is that a high-energy laser beam scans a selected area of the powder bed using a sophisticated optical system. After scanning the layer of powder with the laser, a new powder layer is deposited by a

* Corresponding author.
E-mail address: mbayat@dtu.dk (M. Bayat).

https://doi.org/10.1016/j.jmapro.2023.03.040
Received 19 September 2022; Received in revised form 10 March 2023; Accepted 22 March 2023
Available online 14 April 2023

spreader and the process is repeated until the full part height is printed. The diameter of the laser heat source implemented in the process ranges from about 50 μm to over 300 μm [4] which depends on the type of laser, the optical setup used, and the resulting laser beam quality obtained at the focal plane [5]. As a micron-size laser source is used, high thermal gradients and high solidification and cooling rates are unavoidable [6]. The generation of high thermal gradients also leads to high residual stresses, plastic deformations and under some circumstances, fracture and cracks in the parts [7]. A unique and fine microstructure is created due to the high solidification and cooling rates which determines the mechanical properties of the part [8]. Parts produced by L-PBF can suffer from voids or porosities that are caused either by insufficient or excessive heat input [9]. All these types of defects ultimately deteriorate the mechanical properties of the part and thus additional processes like Hot Isostatic Pressing (HIP) are often needed, thus elongating the process chain [10].

In order to analyse how these defects form and to find a way to mitigate them, an understanding of the active physical mechanisms and their interactions is necessary which can be achieved via in-situ or ex-situ experimentation. In-situ monitoring systems need calibration before the use of the sensors and are expensive to implement [11–13], while using ex-situ tools just provide the outcome of the process for the selected parameters and are also time consuming [9]. To fill this knowledge gap, L-PBF process numerical modelling is a wise choice since it is quite cost-efficient as multiple hypothetical scenarios can be simulated in a short time. The L-PBF process occurs over multiple time and length scales, and hence depending on the type of defects captured, two models namely the part-scale model and meso-scale model [1] could be relevant. The part-scale model simulates the building process of the entire part and captures defects such as residual stresses, deformation, and warping. The meso-scale model simulates the melt pool formation and captures defects such as lack of fusion [14], keyhole induced pores [15] and powder bed denudation [16]. The published literature on meso-scale models of the L-PBF process entails a lot of differences in the assumptions made, frameworks of the models, physics involved, and the methods used for the implementation of the physical phenomena. According to Bayat et al. [1], meso-scale models can be divided into four groups of pure thermal models, thermo-mechanical models, thermo-metallurgical models, and finally fluid-based (computational fluid dynamics – CFD) models. Even the fluid-based meso-scale simulations are sub-divided into specific categories based on their fidelity level [1]. For instance, fluid-based models with flat free surfaces neither account for the recoil pressure nor capillary forces. As an example of this branch of models, Le and Lo [17] developed such a flat-surface CFD simulation for the L-PBF process of 316-L stainless steel where they only took the Marangoni (thermo-capillarity) effect into account, which does not call for any free-surface tracking. Mukherjee et al. [18,19] developed relatively similar CFD models for the L-PBF process of four different alloys and they also ignored the role of recoil pressure and capillarity. It is worth mentioning, that this class of CFD simulations consider the powder layer as a mass- or volume-averaged continuum rather than capturing the shape of every individual powder particles, which is typically done in high-fidelity multi-physics models [20,21]. On the positive side, lower-fidelity simulations such as the mentioned flat-surface CFD models run faster, because of neglecting some of the physics, hence solving for fewer unknown variables, compared to high-fidelity multi-physics simulations. Furthermore, it is computationally efficient to extend low-fidelity continuum simulation models from the meso-scale to part-scale due to reduced geometric complexity as the individual powders are not spatially resolved.

In conduction based meso-scale modelling works like [22–25], the flow of the liquid metal in the melt pool is ignored and the model only solves for the temperature field of the powder bed. By ignoring the fluid flow, the computational time and cost are even further reduced, but the obtained temperature fields are inaccurate, as heat losses due to melt fluid flow convection are ignored [26]. These types of models are only accurate when the melting mode is conduction dominated, hence they fail to capture the well-known keyhole phenomenon, unless very specific calibrated deep heat sources are used [27]. On the other hand, in high-fidelity multi-physics simulation works [28–33], individual powder particles are modelled using the discrete element method (DEM), where the powder particles are spread on a substrate using a roller or a scrapper. This approach is more accurate for modelling the L-PBF process compared to the flat-surface model, since as mentioned earlier, the multi-physics models account for the recoil pressure as well as capillarity. These two mentioned forces play a major role in deciding the shape of the melt pool during the formation and collapse of a keyhole, as noted in welding literature [34–36]. Furthermore, works such as [37] also simulated the gas phase dynamics above the powder bed, while many authors like [16] do not explicitly solve for this, which is also stated in a review paper on meso-scale models of L-PBF [38].

The primary goal of the present paper is to find the ranges of selected material properties and process parameters, where the cheaper, lower-fidelity, flat-surface, thermo-fluid model gives almost the same results as the ones predicted by the high-fidelity multi-physics CFD model. In this work, we quantify the impact of the different interfacial physical phenomena that occur during L-PBF, on the melt pool morphology, and thermal conditions. Therefore, as a first step, a multi-physics numerical model based on the Finite Volume Method (FVM) is developed in the commercial software package Flow-3D using the Weld module for simulating the L-PBF process. The model validation is carried out by comparing the predicted melt pool shape with the ones from in-house single-track experiments. Then we run two sets of simulations with and without consideration of the recoil pressure at different linear energy densities (LED) and at three different beam sizes. This parametric study is carried out to find the LED value below which the recoil pressure can be safely disregarded in such a way that a lower-fidelity flat-surface CFD model gives similar results. This is followed by another parametric study to investigate how different magnitudes of capillary forces affect the melt pool shape and its thermo-fluid conditions. Here the aim is to find the threshold value of surface tension above which the impact of the recoil pressure is negligible. In this part of the investigation, the Marangoni effect is ignored to allow for precise analysis of the opposing interfacial forces of capillarity and the recoil pressure. While doing so, we use the inverse Bond number as the dimensionless variable for quantifying the capillary forces.

2. Model description and L-PBF single-track experiments

2.1. Modelling approach

This section describes the governing equations that are discretized to solve for the various physics involved in the model such as solidification/melting, fluid flow, heat transfer, surface tension, thermo-capillary effects, and evaporation. Below is a list of assumptions made in the model:

- The solver only does calculations for the metal (solid and fluid phase) and does not calculate pressure, velocity, and temperature etc. of the air in the computational domain. Hence, it is a one-phase simulation.
- The metal flow is assumed to be laminar, and the fluid is Newtonian.
- The flow is incompressible and viscous.
- The laser absorptivity is kept constant and does not have a spatial and temporal variation.
- Powder denudation and laser spattering is not captured by the model.
- The laser has a Gaussian planar distribution.
- The powder is spherical in shape and is placed on the substrate by using the rainfall method rather than a physical spreader distributing it.
- The surface tension variation with temperature is linear.

2.1.1. Fluid flow and heat transfer model

The numerical model solves for the temperature and fluid velocity of the metal induced by the heat coming from the laser. Here the equations of continuity and momentum are solved to obtain the velocity and pressure of the molten metal as shown in Eqs. (1) and (2) respectively [14].

$$\nabla.\left(\vec{V}\right) = 0 \tag{1}$$

$$\rho\left[\frac{\partial}{\partial t}\left(\vec{V}\right) + \vec{V}.\nabla\left(\vec{V}\right)\right] = -\nabla p + \nabla.\left[\mu\left(\nabla\vec{V} + \nabla\vec{V}^{T} - \frac{2}{3}\nabla.\vec{V}\right)\right] - \frac{K_c(1-f_l)^2}{C_k + f_l^3}\vec{V} \tag{2}$$

Here V (m/s) is the velocity vector and p (Pa) the pressure field. The second term on the right-hand side of Eq. (2) represents the forces caused by viscous stresses and the third term is the solidification drag force due to the formation of a mushy zone. K_C (kg/m^{3}s) and C_k (−) are the constants used for solidification drag forces and they are typically in the order of 10^6 and 10^{-4}, respectively.

The fluid flow is coupled with the heat transfer via Eq. (3)

$$\rho\left[\frac{\partial}{\partial t}(h) + \vec{V}\cdot\nabla(h)\right] = \nabla\cdot[k_{bulk}(\nabla T)] \tag{3}$$

$$h = h_{ref} + c_{p,bulk}\left(T - T_{ref}\right) + f_l\Delta H_{sl} \tag{4}$$

$$f_l = \begin{cases} 0 & T < T_s \\ \dfrac{T - T_s}{T_l - T_s} & T_s \le T < T_l \\ 1 & T \ge T_l \end{cases} \tag{5}$$

where h (kJ/kg) is the specific enthalpy of the metallic phase, and the subscript 'ref' stands for the reference state from which the enthalpy is evaluated. f_l (−) is the liquid fraction function defined in Eq. (5), which for simplicity is approximated by a linear function of temperature and ΔH_{sl} (kJ/kg) in Eq. (4) is the latent heat of fusion. Here the liquid fraction varies linearly between the solidus and liquidus temperatures.

For the material properties such as density, thermal conductivity and specific heat capacity in the mushy zone, the values are calculated by using linear volumetric-averaging, i.e.:

$$\rho = f_s\rho_s + f_l\rho_l \tag{6}$$

$$k_{bulk} = f_s k_s + f_l k_l \tag{7}$$

$$C_{p,bulk} = \frac{f_s\rho_s c_{p,s} + f_l\rho_l c_{p,l}}{f_s\rho_s + f_l\rho_l} \tag{8}$$

where the subscript 's' refers to solid and 'l' refers to liquid.

In this model, the Volume of Fluid (VOF) method is used to track the free surface of the metal phase. The advantage of using VOF is that the metal-void interface is tracked more accurately as compared to other methods like the Level set method. To calculate the VOF and to capture the interface, the following is used:

$$\frac{\partial}{\partial t}(F) + \nabla.\left(F\vec{V}\right) = 0 \tag{9}$$

where the scalar F (−) is equal to zero and one inside the gaseous and metallic phases respectively. Intermediate values of F indicate an interface between these two immiscible phases. In this work, the calculation for the gas phase is not included because an assumption is made that the gas flow has an insignificant impact on the melt flow characteristics. Hence, the gas phase is treated as a void with no fluid and thermal properties.

2.1.2. The thermo-capillary phenomenon (Marangoni effect)

One of the reasons for the thermo-capillary effect in fluids is the variation of the surface tension with temperature also known as the Marangoni effect, which occurs on the surface of a fluid. Another source is the presence of surface-active elements like oxygen and sulfur, which however is out of the scope of this study but was analyzed by e.g. [39]. The Marangoni effect is accounted for in the model as a shear stress acting on the surface of the molten metal, which causes the molten pool to widen with increasing temperature in the case of a negative surface tension gradient and deepen when the gradient is positive. The change of surface tension with temperature for 316L stainless steel is shown in Table 2. Here the surface tension gradient is active between the liquidus and boiling/evaporation temperature, where the metal is in the fluid state.

2.1.3. Recoil pressure

During processing in L-PBF, a localized laser heat source is used to melt the powder and hence very high temperatures – above 3200 K can be achieved. This high temperature is above the boiling point of the metal and can hence cause local evaporation letting the metal change its phase from liquid to vapor. This vapor phase of metal in turn generates a pressure on the surface of the molten metal, creating a depression zone. By creating this concave depression zone, the laser-material surface area is increased which in turn increases the absolute absorptivity. This pressure is denoted the recoil pressure and is accounted for in the model as a pressure acting perpendicularly to the free surface without implicitly modelling the liquid to vapor phase transition. In summary, the recoil pressure, Marangoni shear force, and surface tension are all acting on the free surface interface and are expressed by

$$F_{V/F}(Pa) = [P_{recoil} + \sigma.\kappa]\vec{n} + [\nabla T - \vec{n}(\nabla T.\vec{n})]\frac{d\sigma}{dT}. \tag{10}$$

The second expression on the right-hand side of Eq. (10) is the Marangoni shear stress and $-d\sigma/dT$ (kg.s^2.K^{-1}) represents the dependency of surface tension on temperature and acts tangential to the free surface of the fluid. P_{recoil} (Pa) is the pressure acting normal to the free surface of the melt pool when it is overheated above the boiling point of the metal and κ (m^{-1}) is the curvature of the free surface of the fluid, whereas 'n' denotes the normal direction to the interface.

The recoil pressure in the first term Eq. (10) can be expressed by

$$P_{recoil}(T) = 0.54P_{atm}e^{\left[\frac{\Delta H_{lv}}{C_v(\gamma-1)}\left(\frac{1}{T_g}-\frac{1}{T}\right)\right]} \tag{11}$$

This is further simplified by compounding constants together as shown in Eqs. (12), (13) and (14).

$$P_{recoil}(T) = Ae^{\left\{B\left(1-\frac{T_v}{T}\right)\right\}}, \tag{12}$$

wherein

$$A = 0.54P_{atm} \tag{13}$$

$$B = \frac{\Delta H_v}{(\gamma-1)c_v T_v} \tag{14}$$

2.1.4. Ray tracing with multiple reflections

The heat source in the model is a laser spot with a predefined diameter that traverses along the powder bed with a particular scanning speed. This laser spot generates an input heat flux into the computational domain and varies spatially from the center axis of the laser according to Eq. (15).

$$q''_{laser}(x,y) = \frac{2P}{\pi R^2} e^{\left(-\frac{2\left((x-x_{las})^2+(y-y_{las})^2\right)}{R^2} \right)} \quad (15)$$

where P (W), R (m), x_{las} (m) and y_{las} (m) are laser power, laser beam spot radius, x coordinate and y coordinate of the initial laser position. When the laser is traversing in a straight line in the x direction, y is equal to 0 and x is equal to $v \cdot t$, where v is the laser scanning speed and t is time. The laser spot has a planar Gaussian distribution of heat flux into the domain and is discretized according to the mesh size used. The discretized heat flux i.e., the heat source used in the numerical solution when compared with the analytical model can be graphically explained in Fig. 1(b).

The choice of cell size determines the discretization of the laser heat flux as well as the number of rays being generated. As depicted in Fig. 1 (a), the incident ray $r_{i,j}$ from the laser undergoes multiple reflections in the vapor depression zone and upon every interaction of the ray with the molten metal, the energy of the ray is reduced. The surface normal vector 'n' is defined with respect to the fluid's surface. More details on the ray tracing algorithm applied in L-PBF can be found in the previous works by the author group [14].

2.1.5. Powder bed model

In order to obtain the geometry of the powder layer which will be treated as a fluid region in the thermal-CFD simulations, the Discrete Element Method (DEM) is used. The basic framework of how DEM works is shown in Fig. 1(c) with an example of collision between two particles. As DEM is formulated in a Lagrangian framework, each powder particle is modelled as a sphere and the powder motion is governed by Newton's second law. The location and velocity of the individual particles are tracked as they move through a pre-defined numerical domain. The Hertz-Mindlin contact model is used to define the mechanics when the particle encounters another particle or a wall. In this contact model, the sphere is treated as a spring and damper system, which is used to calculate the resulting forces $F_{a,N}$, $F_{a,T}$, $F_{b,N}$ and $F_{b,T}$ for particles A and B, when they collide into each another. The $d_{overlap}$ distance is an input to the model and is generally a factor less than one times the diameter. To model the rotational and translational frictional forces, a frictional contact is modelled, which links the two spring and damper systems of both the particles in the mathematical model. The value of the coefficient of friction μ (−) is calibrated by experimental tests such as the dynamic and static angle of repose test as well as the Hall flow test. The above mentioned DEM methodology and simulation framework of powder spreading on a substrate with different spreader speeds [40], shape of spreader [41] and the type of the spreader was thoroughly worked upon in literature [42–45].

When this numerical method is applied in L-PBF, spherical powder particles are dropped from the top of the domain which is usually denoted as the 'rain-drop' method. The approach was e.g. used for modelling of additive manufacturing by [46] where a Lattice–Boltzmann method was applied to model the melting and solidification of a multi-layer L-PBF process. The bottom and the side faces of the domain are treated as walls. However, as the 'rain-drop' method is used for powder deposition, the model does not need calibration from experimental tests unlike the models where a scrapper or roller is used to deposit a powder layer [47]. This method of powder deposition is extremely computationally efficient, as compared to modelling the actual scrapping of a powder bed using a roller or a spreader. The powder generation is stopped as soon as the pre-determined powder layer thickness of 45 μm is obtained. The particle size distribution (PSD)

Table 1
Powder size distribution of SS 316L gas-atomized powder.

Powder size (μm) <	Average powder size (μm)	Cumulative %
20	15	3.77
25	23	15.54
30	27	35.18
35	33	56.47
40	37	75.48
45	43	90.14
50	47	100.00

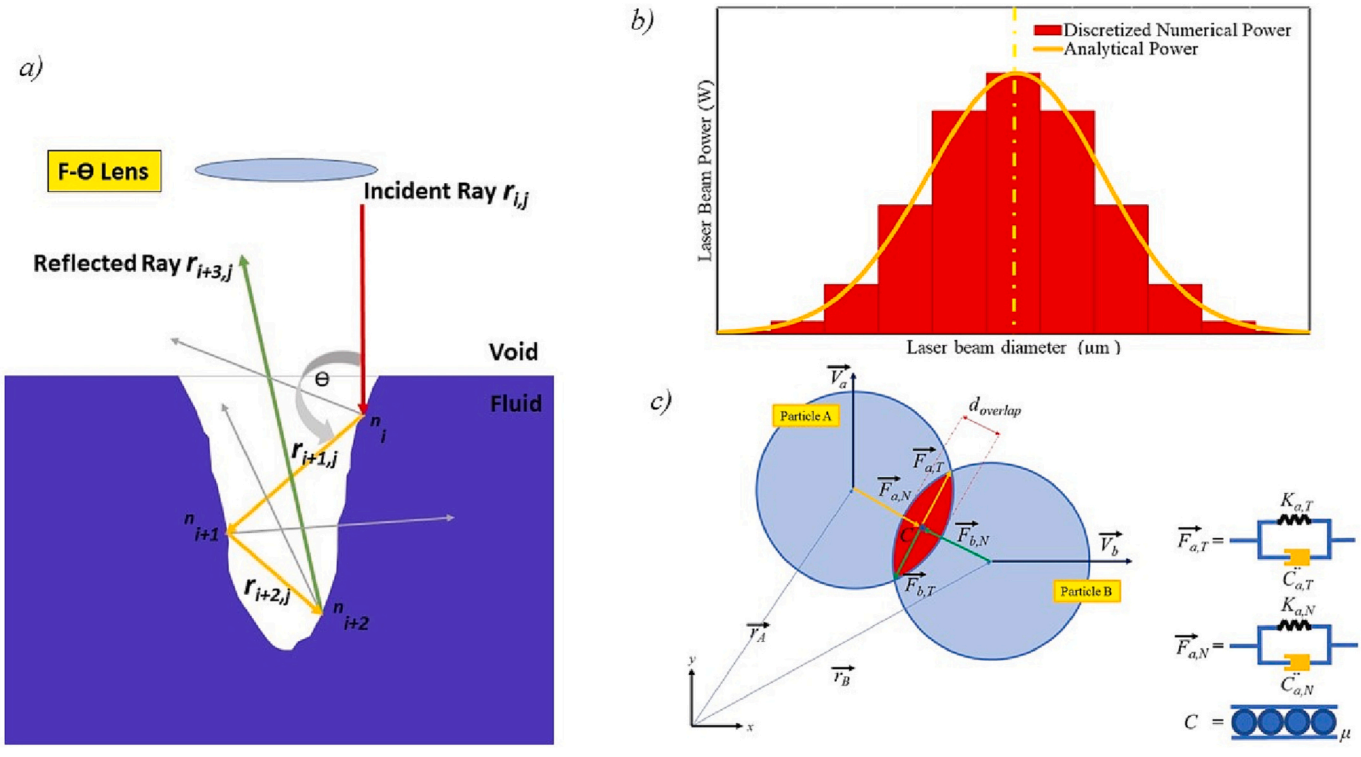

Fig. 1. a) Multiple reflections of laser rays in vapor depression b) discretization of Gaussian laser intensity c) Mechanics in the Discrete Element Method (DEM).

to be used in the model is obtained from the powder manufacturer and is shown in Table 1, where also an average particle size for each powder size range is assumed. This average powder size is used in the DEM model and is also displayed in Fig. 2, where both the variation of volume % and the cumulative % are plotted.

The above-mentioned PSD along with the Young's Modulus and Poisson's ratio for 316L powders are imported into the Hertz-Mindlin contact model. The number of particles added to the domain also known as the powder generation rate was varied to achieve a packed powder layer thickness of 45 μm. Fig. 3 shows the variation of particle generation rate to powder layer thickness. It is found that using a powder generation rate of 720 particles per second (marked with the blue circle), a dense powder bed is achieved with a powder layer thickness of 45 μm, which is very close to the nominal layer thickness. Once the powder bed is created, the powder bed geometry is imported into the FVM based thermal-CFD simulation setup as part of the fluid region, however initially in solid state.

2.1.6. Numerical domain and boundary conditions

The numerical domain size is 1100 μm × 500 μm × 350 μm for the single-track models. The substrate is 200 μm thick and has a powder layer thickness of 45 μm as shown in Fig. 3. The material assigned to the powder bed and substrate is 316L stainless steel. The numerical domain used in the simulations is shown in Fig. 4 along with the direction of the linear laser motion. The computational domain, contains a void region which is 150 μm in height from the top surface of the bulk region so the movement of the free surface interface must be tracked. Fig. 4(a) shows the computational domain with boundaries and (b) shows the same computational domain discretized with a mesh cell size of 5 μm. This cell size is selected based on a mesh independency study and is conducted for the single-track process condition in Section 3.

The Marangoni shear force, recoil pressure and all other forces as described in Eq. (10) are applied on the free surface of the melt pool. The thermal boundary condition applied on the exposed surface of the metal is given as

$$-k\frac{\partial T}{\partial \vec{n}} = \varepsilon\sigma_{rad}\left(T_{amb}^4 - T^4\right) + h_{amb}\left(T_{amb} - T\right) - q''_{laser} + q''_{evap} \quad (16)$$

where, ε (−) and σ_{rad} (W/m^2/K^4) represent the emissivity and Stephan-Boltzmann constants respectively, h_{amb} (W/m^2/K) represents convective heat transfer coefficient, q''_{laser} (W.m^{-2}) is the input heat flux from the laser and q_{vap} is the heat loss due to vaporization. More information about the thermal boundary conditions on the free surface can be found in the previous works by the author group [15].

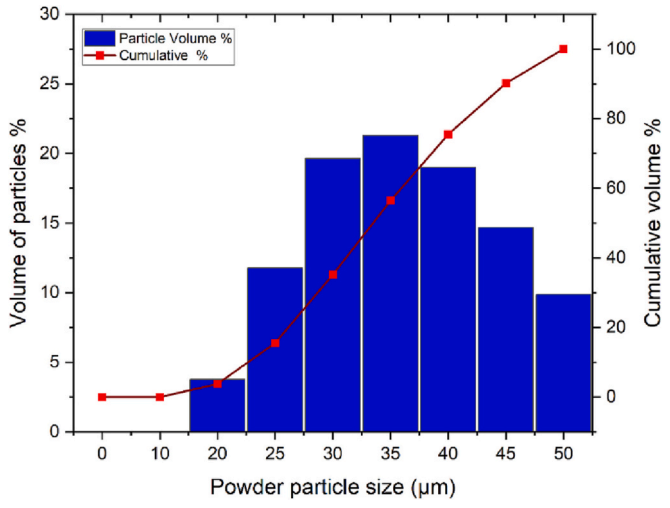

Fig. 2. Powder size distribution (PSD) of stainless-steel gas-atomized 316L powder used in the DEM numerical model.

The side, bottom and top walls of the numerical domain were set as an adiabatic, continuative and pressure outlet condition respectively. The domain is set sufficiently wide, such that the effects of the side wall conditions have minimal impact on the temperature values.

2.2. Experiments

To ensure a proper calibration of the multi-physics numerical model, individual single line-track test-samples were printed with a SISMA Mysint100 (Sisma S.p.A, Italy) L-PBF machine equipped with a fiber laser producing a maximum power of 200 W. Gas atomized stainless steel 316L powder was used to create the powder bedon a small substrate cube of 6 mm × 3 mm × 5 mm. The printing parameters were the default parameters by the L-PBF machine manufacturer for 316L powder, with a scanning speed of 1.5 m/s, a power of 120 W, a layer height of 30 μm and a laser spot radius of 15 μm. The parameters of the single track were kept fixed to the default parameters, where only the scanning speed and laser power were changed to 0.5 m/s and 80 W. After the build, the test-sample was removed from the base plate, sonicated and dried with pressurised air to remove residual powder particles. Prior to the optical microscope measurement to obtain the key melt-pool parameters (height and width), the sample was immersed in resin to allow for proper polishing. The side of the cube perpendicular to the line tracks was polished to remove the end section of the tracks. Subsequently, the polished side was etched for 5 min with 5 % Nital solution to visualize the edges of the melt pools.

The melt pool geometry from the single-track experiment was captured by a 3D optical profiler (Sensofar Plu Neox, Sensofar, Spain) operating in confocal mode with a 20× magnification objective [48]. More specifically, the provided operation software was used to measure the melt-pool dimensions of a single line track to obtain the melt-pool-depth and -width and the result is shown in Table 3. In this study for validating the numerical model only the first track results are used.

3. Validation

In order to check that the numerical model replicates the process conditions and the resulting geometry of the melt pool, a validation step is necessary before conducting the parametric analysis. In the validation, the simulated melt pool shape as well as its dimensions from the calibrated numerical model is compared to the experiment, see.

Table 3. The numerical model is run with the same process parameters as the experiments given in Table 2 and a 2D melt pool contour was taken at a location where the melt pool had reached a pseudo-steady state, i.e. the variation in melt pool depth does not vary with further laser travel. The cross-section/lateral plane location in the validation case for the model is taken 500 μm (x-direction as shown in Fig. 4(a)) from the laser starting position and this position can change depending on the chosen laser process parameters. A cubic mesh is used to discretize the computational domain as shown in Fig. 4(b) and the size of the cells is decided through a mesh independency test. In this test, a set of numerical calculation cases were solved with the same process parameters except the mesh cell size was varied from 8 μm to 4 μm and the simulation output i.e., melt pool depth and width were reported. More details about this test can be found in [49]. A cell size of 5 μm was chosen, since it provided a computationally efficient and converged result.

As seen in Fig. 5, the simulated melt pool matches very well with the experiments and the reason for this should be found in the fact that the numerical model accounts for all three major physical phenomena occurring in the melt pool during the L-PBF process. The error in the melt pool depth and width is roughly two times the mesh cell size and can be attributed to the assumptions made in the model in Section 2.1. For example, the melt pool height was not used as a measure to validate the model, due to powder spattering effects during the laser processing which were not accounted by the numerical model. Moreover, also the

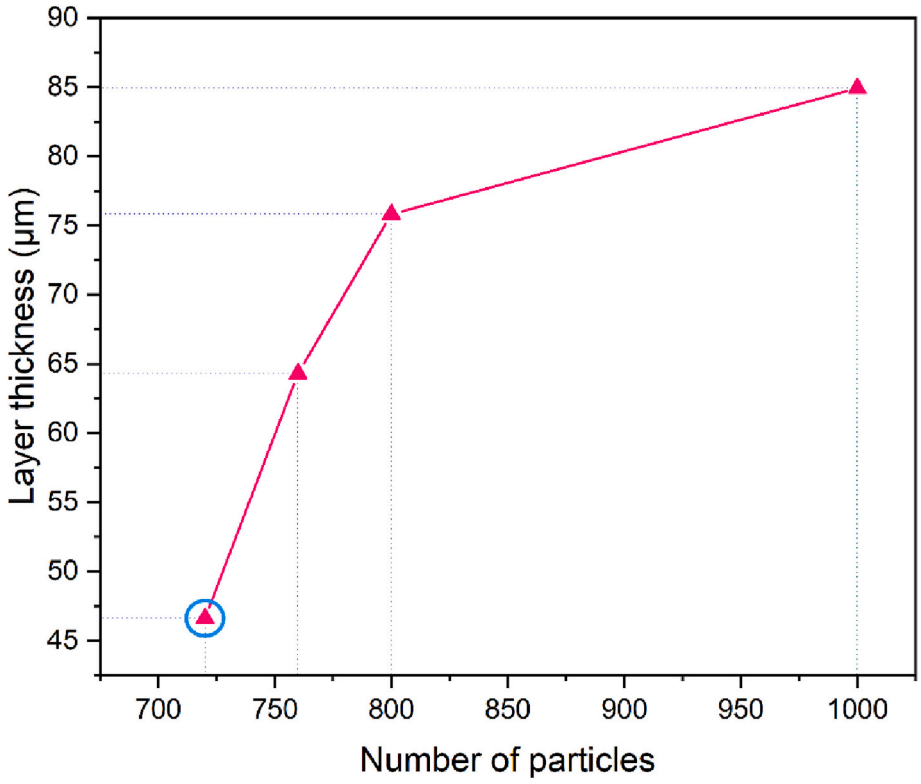

Fig. 3. Variation in powder bed layer thickness with number of particles present in the numerical domain generated using the Rainfall method. When the number of particles is 720, a powder bed layer thickness of 45 μm is created and this data point is marked by a blue circle. (For interpretation of the references to color in this figure legend, the reader is referred to the web version of this article.)

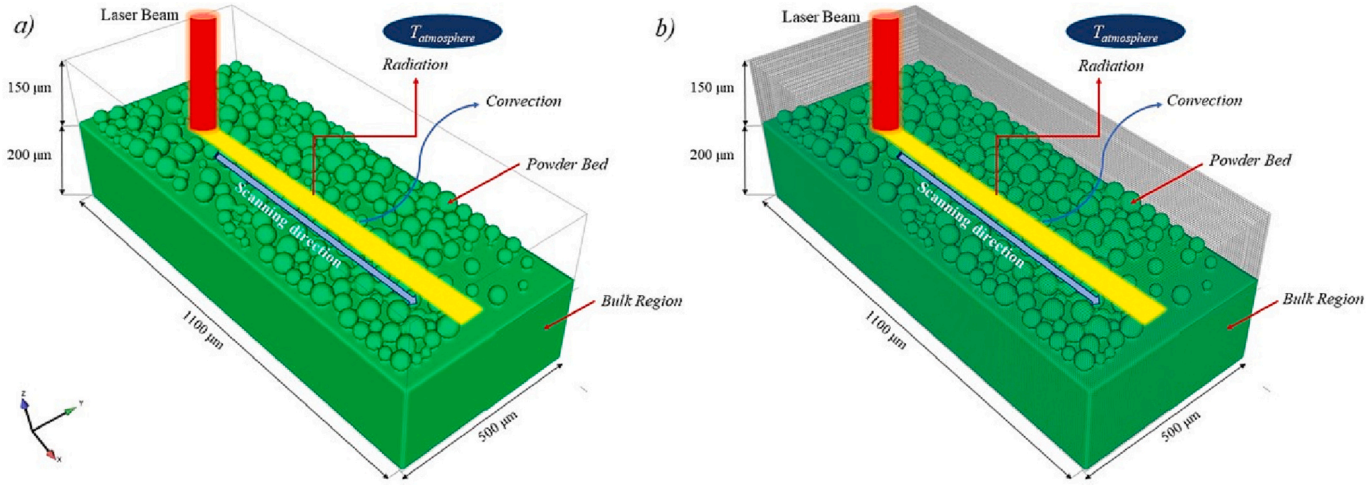

Fig. 4. Framework for single laser track simulation model including powder bed and substrate (a) computational domain with boundaries (b) discretization of the domain with uniform quad mesh.

stochastic nature of the powder bed morphology shows some effect, since it is impossible to obtain the same particle diameter-distribution that was present in the experiment. The powder spattering is caused by the development of a vapor plume from the melt pool surface when a temperature above the boiling point is achieved. The vapor plume interacts with the surrounding atmosphere to create an entrained gas flow that drags the surrounding powder particles into the laser-material interaction zone [50].

4. Results and discussion

The validated model is subsequently used for parametric study cases of the recoil pressure and the surface tension at different melt pool regimes by implementing different laser energy densities. These sensitivity studies provide in turn a window of possible process parameters where one could replace a lower fidelity, low-cost, flat surface model instead of a multi-physics model within that specific window.

Table 2
Thermo-physical properties of 316L stainless steel and L-PBF process parameters. * shows laser process parameters namely the laser power and scanning speed which were used to print the bulk material.

Parameter	Symbol	Value	Units
Density at room temperature	ρ	7900	kg/m^3
Viscosity	μ	0.6	kg/m/s
Liquidus temperature	T_l	1733	K
Solidus temperature	T_s	1693	K
Boiling temperature	T_b	3200	K
Latent heat of fusion	ΔH_{sl}	$0.272{\cdot}10^6$	J/kg
Latent heat of evaporation	ΔH_{lv}	$6.46{\cdot}10^6$	J/kg
Ambient convective heat transfer	h_{amb}	80	W/m^2.K
Surface tension gradient [49]	γ	−0.0008	kg/s^2/K
Surface tension at liquidus temperature	σ	0.3282	kg/s^2
Thermal conductivity in solid state	k_s	13.96	W/m.K
Thermal conductivity in liquid state	k_l	35.95	W/m.K
Specific heat capacity in solid state	$c_{p,s}$	434	J/kg.K
Specific heat capacity in liquid state	$c_{p,l}$	965	J/kg.K
Surface emissivity	ε	0.4	–
Laser power	P	120*/80	W
Scanning speed	v	1500*/500	mm/s
Layer thickness	t	45	μm
Beam spot size	r_b	15	μm

Table 3
Experimental melt pool dimensions in a lateral cross-section to the laser scanning direction measured through microscope images.

Track no.	Melt pool width (μm)	Melt pool depth (μm)
1	110.4	114.6
2	120.3	113.9

Table 4
Process parameters used in the recoil pressure sensitivity study.

Laser power (W)	40	80	140	200
Scanning speed (m/s)	0.5			
LED (J/m)	80	160	280	400
Beam diameter (μm)	20	60	120	

4.1. Sensitivity of recoil pressure

As mentioned in Section 2.1.3, the recoil pressure is the vapor pressure generated on the melt pool due to overheating of the melt pool above the boiling temperature. This makes the melt pool deeper and increases the absorption in the laser-material interaction zone due to the ray trapping as a result of the multiple reflection effect as explained in Section 2.1.4. The presence of recoil pressure adds momentum to the fluid flow by depressing the free surface of the melt pool.

In the first part of the parametric study, the LED as a condensed process parameter is used, which basically condenses the two important laser parameters of power and scanning speed into one parameter. The LED is varied from 80 to 400 J/m while the laser beam spot diameter is varied from 20 μm to 120 μm. Two scenarios are considered, where the first will account for the recoil pressure while the other will not. The main aim of this sensitivity study is to obtain a threshold value of the LED for each beam size, below which the presence of recoil pressure can be ignored. This can be beneficial for MAM users who would like to define a process window for new potential alloys that can be manufactured by MAM using numerical simulation tools due to their advantages as discussed in Section 1.

The values of the laser process parameters are shown in Table 4, wherein a total of 24 simulations were carried out (12 cases with the absence of Recoil pressure and 12 cases with the presence of recoil pressure), and the respective thermo-fluid data such as temperature, velocity etc. were post-processed after the single-track was solidified. The melt pool shape and size were analyzed at a fixed location where the size of the melt pool attained a pseudo-steady state. The measured melt pool depth and the LED values are plotted in Fig. 6 for the beam diameters 20 μm, 60 μm and 120 μm considered in this study. When ignoring recoil pressure from the calculation, the predicted melt pool dimensions are for certain parameters similar to the cases where the recoil pressure was taken into account. More specifically, this highly depends on the laser beam size and the LED values used in the single-track process. For a laser beam size of 20 μm, the predicted melt pool depth is nearly identical for the 'No recoil' and 'recoil' cases when the LED is 80 J/m or lower. For a laser beam size of 60 μm and 120 μm this threshold LED is 160 and 280 J/m respectively. These threshold LED values are circled in Fig. 6 and a trend can be noted that as the laser beam size increases, the threshold LED shifts towards a higher value. This indicates that for all the laser beam sizes in the range of 20 μm to 120 μm, there is a specific LED value, below which the recoil pressure is insignificant and can be ignored from the model. This suggests that a lower-fidelity model, ignoring the recoil pressure, can replace multi-physics models in these ranges. Furthermore, the no-recoil assumption holds for a wider range at bigger beam sizes and only slightly diverges at higher LED values from the with-recoil case prediction. This is mainly because, as expected, the laser intensity is higher for smaller beam sizes, thus larger heat fluxes form which consequently lead to bigger and deeper depressions that the no-recoil cases fail to predict.

To compare the melt pool shape and size, 2D melt pool contours are displayed in Fig. 7 for four LED values, where laser beam diameters of 20 μm, 60 μm and 120 μm were used in the simulations with and without applying recoil pressure in the model. The contour plane is perpendicular to the laser traveling direction, i.e. being the y-z plane. The green region is the melt pool profile which is obtained when the recoil pressure is absent, and the red region is where the recoil pressure is present. The green and red color regions represent the regions of the substrate and powder bed that have undergone melting and subsequent solidification during the single-track L-PBF. The blue region is the non-melted zone of the computational domain for both cases.

It can instantly be observed that for all cases where recoil pressure is absent, the melt pool depth is lower than the cases in which it is present. The difference in melt pool dimension and the significance of recoil in the model reduces significantly with the increase in laser beam size. This is because by using larger beam sizes, the irradiation area on the powder bed is increased, but the laser radiation intensity is reduced, since the overall heat input is preserved. Laser radiation intensity is the ratio of laser power and irradiation area. Thus, by increasing the LED value by increasing the power at a fixed laser scanning speed, the melt pool volume increases. In this study, for smaller beam sizes like 20 μm, the recoil pressure is quite significant because the laser intensity is higher at this beam size and the heat input superheats the melt pool above the boiling point of the material. The evaporation of the metal creates a depression zone at the laser beam melt pool interface and dynamically increases the absorptivity of the laser heat flux into the material due to the multiple reflection effect. If this depression zone is not accounted for in the model, it can lead to underestimation of the melt pool temperature due to higher laser radiation being reflected out of the domain as the keyhole is not sufficiently deep to trap the laser rays. Hence, the threshold LED must be calculated for a laser beam size in order to prevent incorrect predictions. The error in melt pool size is bigger when the laser beam size is small. For comparison, when a laser beam size of 20 μm is used at an LED value of 280 J/m, which is greater than the threshold value of 80 J/m, the error in the predicted depth is increases when ignoring the recoil pressure in the calculation . But if the laser beam size is increased to 60 μm and an LED value of 400 J/m is used, which is 240 J/m higher than the actual LED threshold, the error in melt pool depth prediction is lower. Therefore, as the laser beam size is increased, the degree of under-prediction of the melt pool depth in recoil pressure absent cases decreases as well.

A 3D temperature contour for the four LED values 80, 160, 280 and 400 J/m at the laser beam size of 120 μm with and without recoil

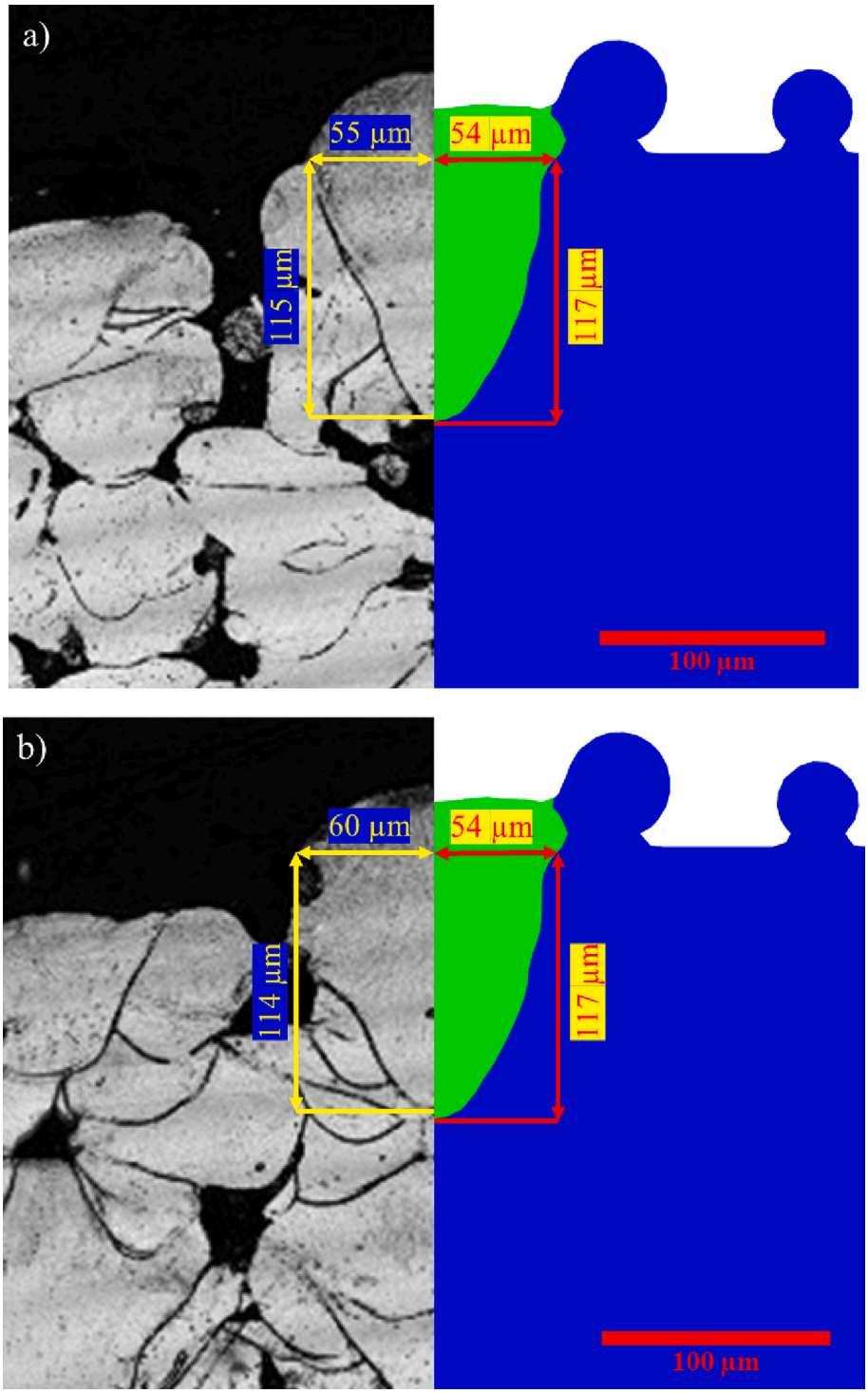

Fig. 5. Experimental melt pool (left) compared to the simulated melt pool (right) along with the melt pool dimensions for (a) Track-01 and (b) Track-02, where the process parameters mentioned in Table 2 were used.

pressure is shown in Fig. 8.

From Fig. 8 it can be observed that the significance of recoil pressure on the temperature distribution is negligible for the LED values 80, 160 and 280 J/m, when a laser beam size of 120 µm is used. This indicates that at higher laser beam sizes, evaporation from the melt pool is very small and therefore the recoil pressure has less impact on the thermo-fluid conditions. Therefore, ignoring the recoil pressure generating this depression, does not affect the melt pool size and shape prediction and this allows for using lower fidelity models without recoil pressure, while still obtaining equally accurate results as if using a multi-physics model including the recoil pressure.

There is a depression on the melt pool surface at the laser-material interaction irrespective of the inclusion of recoil pressure in the calculation. The volume of fluid (VOF) method is used for free surface tracking and is expressed by Eq. (9), in which the surface tension forces, Marangoni shear stress, and recoil pressure are acting. In Fig. 8, Marangoni convection and atmospheric pressure, cause the depression and have higher influence on the melt pool dynamics, when large beam

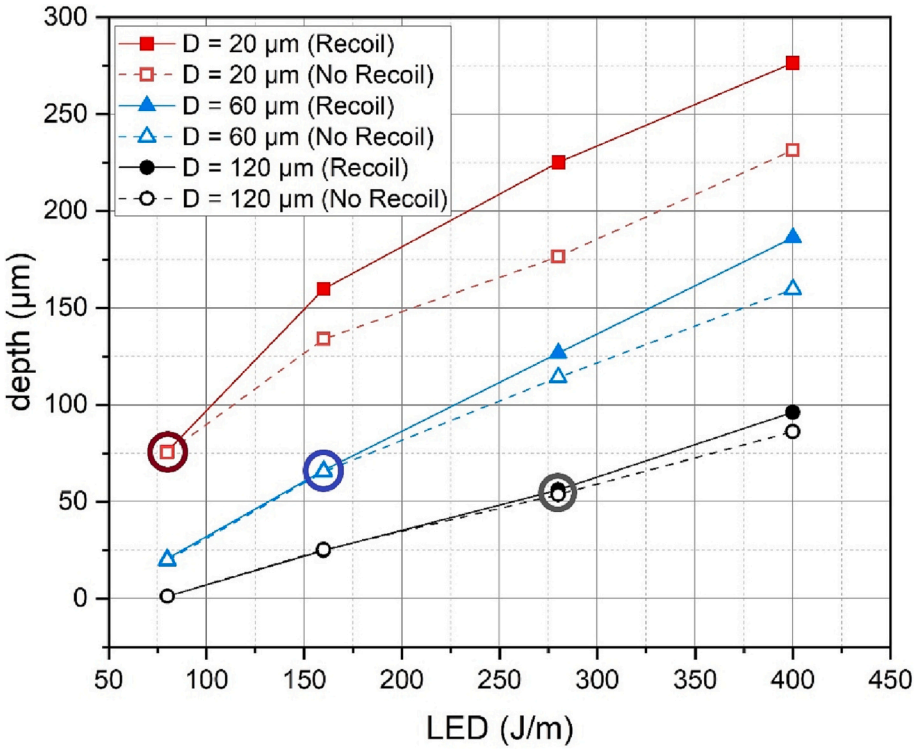

Fig. 6. Melt pool depth for laser beam diameters of 20 µm, 60 µm and 120 µm each for LED values of 80 J/m, 160 J/m, 280 J/m and 400 J/m with and without recoil.

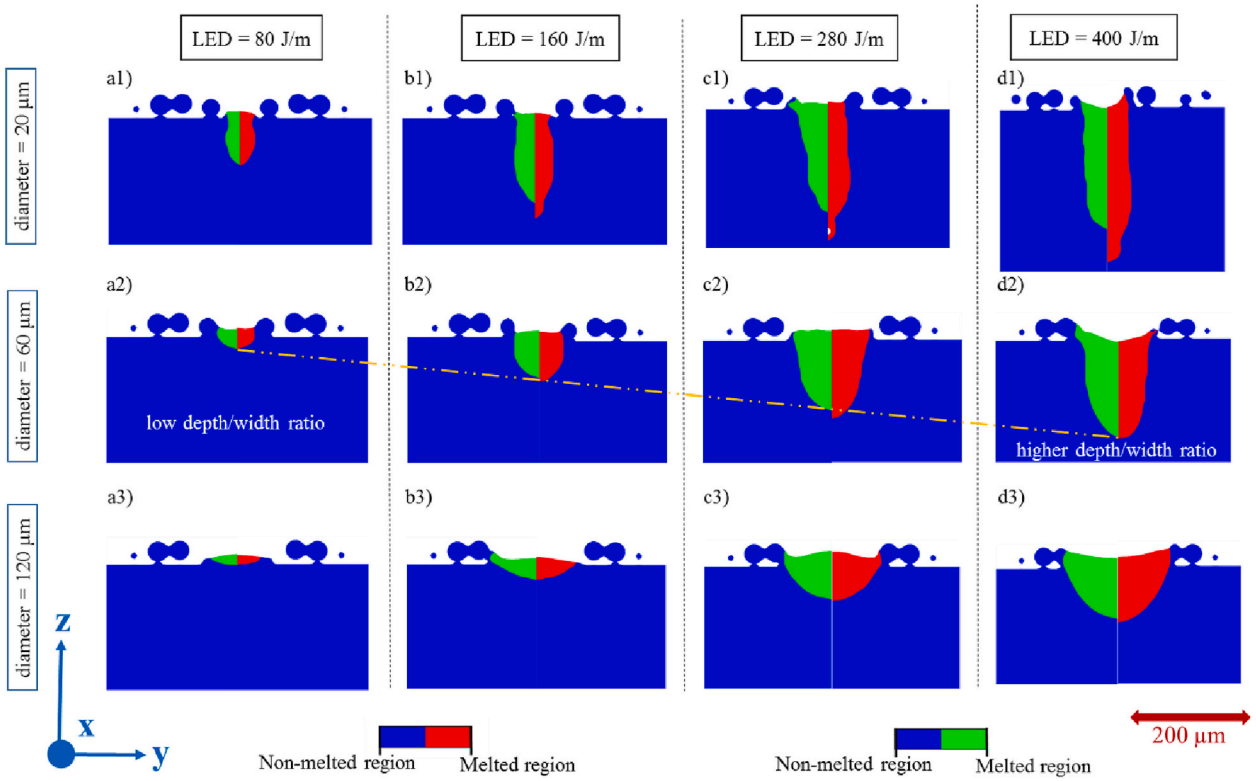

Fig. 7. 2D melt pool contours for three laser beam diameters which are 20 µm, 60 µm, and 120 µm and four LED values a1–a3) 80, b1–b3) 160, c1–c3) 280 and d1–d3) 400 J/m when the melt pool reaches a pseudo-steady state. The colors red and green indicate the melted regions when recoil is present and absent in the numerical model, respectively while the non-melted region is indicated by blue color. The increase in melt pool depth with the LED values for both recoil absent and recoil present cases is also shown for laser beam diameter of 60 µm with a yellow dotted line. (For interpretation of the references to color in this figure legend, the reader is referred to the web version of this article.)

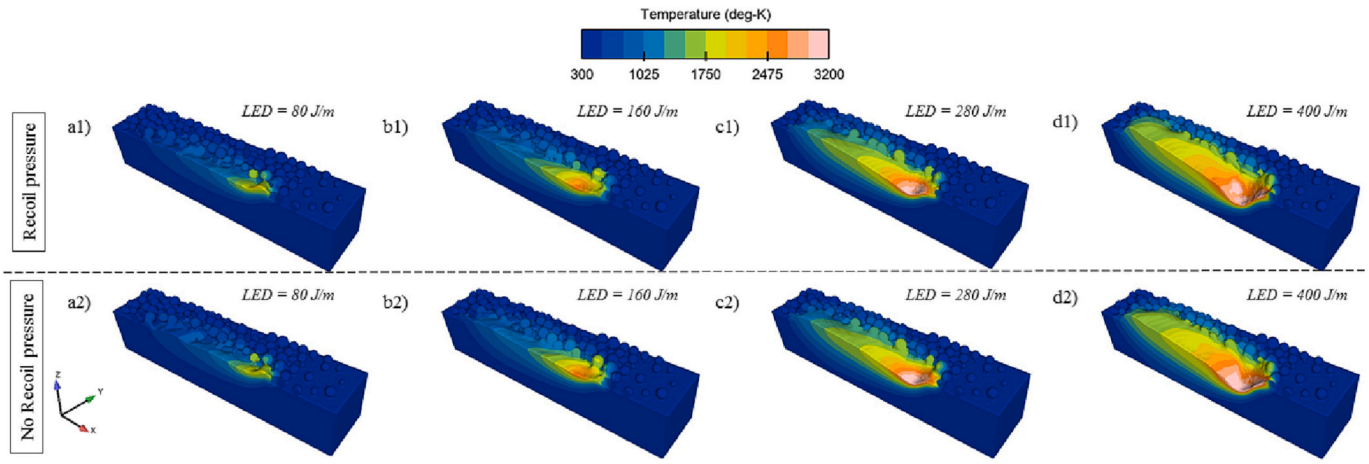

Fig. 8. 3D temperature plots at time = 1.2 μs during the single-track formation on the powder bed with four energy densities values a1–a2) 80 J/m, b1–b2) 160 J/m, c1–c2) 280 J/m and d1–d2) 400 J/m *with* and *without* recoil pressure in the model. A laser beam diameter of 120 um was used for the single-track numerical simulation.

diameters are used. When the LED is increased more heat is absorbed by the metal increasing its temperature of the molten metal and thus reducing the surface tension. As there is a gradient of temperature on the melt pool surface due to a moving heat source a gradient in surface tension is also created on the top surface of the melt pool. This leads to fluid flowing from the center of the melt pool where the temperature is the highest, to the sides and the tail of the melt pool where it is colder. For the atmospheric pressure on top the melt pool, the decrease of surface tension with increase in temperature as explained in Section 2.1.2, leads to the direct irradiated zone of the melt pool to have a lower surface tension. The atmospheric pressure and surface tension force oppose each other on the surface of the melt pool. As the surface tension is reduced in the melt pool due to temperature rise, the result is a depression zone ensuring equilibrium between the two opposite acting forces. Thus, a further increase of an already large beam will reduce the relative influence of recoil pressure and correspondingly increase the effect of surface tension and Marangoni shear stress on the melt pool dynamics.

4.2. Surface tension (the capillary force)

In general, the Marangoni shear stress acts on the melt pool surface due to the surface tension gradient caused by temperature changes. In the present case, this shear stress creates a convection current in the melt pool, where the molten metal from the high temperature region near the laser-material interaction zone is transported to the colder regions.

In order to investigate the independent role of capillarity on the melt pool shape and its thermo-fluid conditions, the Marangoni effect is ignored here, and therefore a constant surface tension value is used over the melting temperature range. Hence the third term in Eq. (10) is set to zero. Ten different surface tension values are used ranging from 0.005 kg/s^2 to 10 kg/s^2, while applying the nominal process parameters used earlier in the validation study. The constant surface tension values are 0.005, 0.05, 0.1, 0.25, 0.5, 1, 2.5, 5, 7.5 and 10 kg/s^2 in this parametric study.

Two dimensionless numbers are introduced in this sensitivity study for the purpose of elucidating which phenomenon is dominant under different surface tension conditions. The first one is the Bond number *Bo* (−) which is the ratio of gravitational to surface tension forces.

$$\mathrm{Bo} = \frac{\rho \vec{g} l^2}{\sigma}, \tag{17}$$

where ρ (kg/m^3) is the density of the fluid, g (m/s^2) is the gravitation constant, σ (kg/s^2) is the surface tension, and l (m) is the characteristic length of the melt pool. The details of the characteristic length measurement can be found in [49].

The second number introduced is the Nusselt number *Nu* (−) and it is defined as follows

$$\mathrm{Nu} = \frac{\mathrm{hl}}{\mathrm{k_f}}, \tag{18}$$

where h (W/m^{2}K) is the melt pool's convective heat transfer coefficient, k_f (W/m K) is thermal conductivity in the fluid and l (m) is the characteristic length, in this case the length of the melt pool [49].

For all temperature independent surface tension cases in the sensitivity study, 3D temperature contours including fluid flow velocity vectors are displayed in Fig. 9 at 1.2 μs, which is a point in time where the melt pool has reached its quasi-steady state. A 2D inset image for each case is also included, which shows the created melt pool indicted by the red color region in the red-blue color contour plot, while the blue color indicates the un-melted regions. The inspection plane A-A' is at a location where the melt pool has attained a pseudo-steady state along the laser scanning direction as well. When the surface tension is below 2.5 kg/s^2, the deep and narrow melt pools are predicted as shown in Fig. 9(a–f), indicating that the melt pool dynamics are dominated by recoil pressure, where the high density of velocity vectors provides an initial indication that convection could be the dominating heat transfer mechanism.

In the extreme case where the lowest surface tension 0.005 kg/s^2 is used, spatter is created due to the increase in wettability of the molten material with reduced surface tension. This phenomenon, coupled with the high recoil pressure, causes the molten material with a high momentum to break into droplets, whenever the momentum is high enough to overcome the cohesive surface tension force. In addition, spattering also leads to instability and fluctuations in the penetration depth of the melt pool due to sudden mass and energy loss from the melt pool. The sudden variation in the shape and size of the depression zone also leads to a variation in the efficiency of the energy coupling in the laser material interaction, which can be explained by the multiple reflection phenomenon described in Section 2.1.4. Thus, the energy absorbed by the material is not constant and this leads to melt pool instability. Increasing the surface tension to 0.05 kg/s^2 suppresses the spatter formation and the formed vapor depression becomes stable along the length of the scanned track. The volume of the melt pool is also increased with a surface tension from 0.05 kg/s^2 to 1 kg/s^2, wherein a stable keyhole depression is formed indicated by the 1750 K temperature isocontour in Fig. 9(b–e). The angle between the keyhole front and back wall also reduces with an increase in surface tension from 0.005

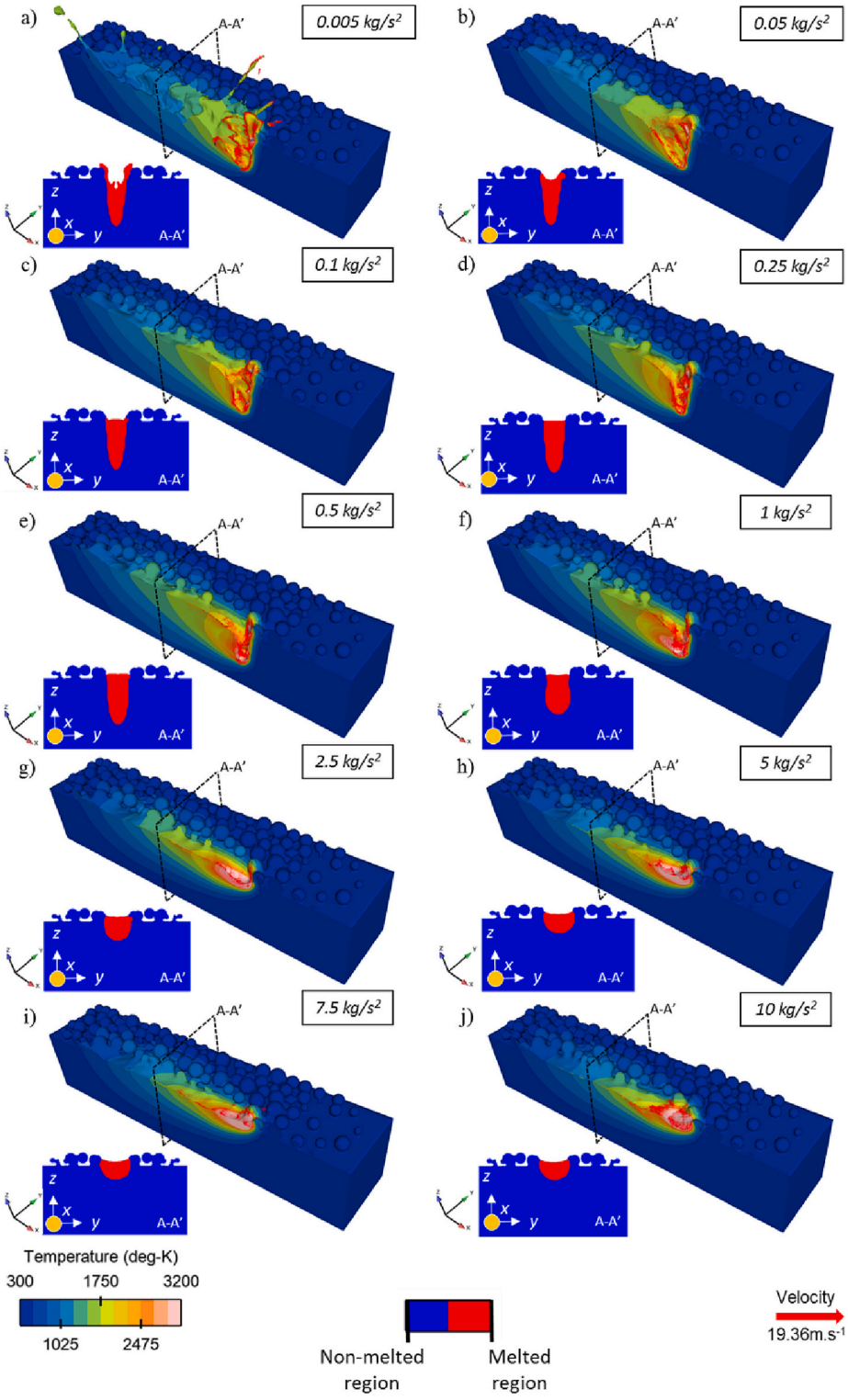

Fig. 9. 3D temperature contour plots of half the computational domain at $t = 1.2$ μs of cases with temperature independent surface tension values a) 0.005 kg/s^2 b) 0.05 kg/s^2 c) 0.1 kg/s^2 d) 0.25 kg/s^2 e) 0.5 kg/s^2 f) 1 kg/s^2 g) 2.5 kg/s^2 h) 5 kg/s^2 i) 7.5 kg/s^2 j) 10 kg/s^2. For each case, the melt pool morphology is displayed at a pseudo-steady state in the inset images. The red regions in these images indicate the melt pool, while the blue region indicates un-melted zones. (For interpretation of the references to color in this figure legend, the reader is referred to the web version of this article.)

kg/s^2 to 1 kg/s^2 and a further increase in surface tension eliminates the depression zone. As the surface tension increases from 0.05 kg/s^2 to 1 kg/s^2 the molten material at the back wall of the depression zone accumulates and a hump forms reducing the angle between the keyhole walls [51]. This indirectly increases the absorption of the laser radiation through ray trapping and more heat is added to the melt pool, thus raising the temperature as seen when comparing the temperature plots from Fig. 9(b–e) in which a small amount of the isocontour in the temperature range of 1750 K to 2475 K is present for a surface tension of 0.05 kg/s^2.

A decreasing trend in the predicted melt pool velocity is shown in Fig. 9(b–f), where the average velocity decreases with increasing the surface tension from 0.005 kg/s^2 to 1 kg/s^2. Due to the increase in the molten material region behind the laser heating zone, the directly laser irradiated molten material could form vortices and dissipate heat through convection. With an increase in surface tension there is a retardation of the fluid flow motion, increasing the resistance to flow and thus decreasing the average fluid flow velocity. This lack of fluid

motion in the melt pool changes the mechanism of heat transfer towards conduction accompanied with heat accumulation. This could also alter the solidification parameters like solidification temperature gradients (K. m^{-1}) and cooling rates (K.s^{-1}), which ultimately affects the microstructure characteristics like grain size and morphology [52].

From Fig. 10 a global trend is clearly observed that as the inverse of *Bo* increases, the depth/width ratio of the melt pool decreases. In low surface tension cases where the melt pool depth/width ratio is high, a keyhole melting mode is established and in this mode the melt pool dynamic is governed by the recoil pressure. Hence this recoil pressure dominant region is marked by red color in Fig. 10 and the surface tension values that are included in this region are 0.005, 0.05, 0.1, 0.25, 0.5 and 1 kg/s^2. The melt pool morphology and thermo-fluid conditions for these recoil dominant cases can be seen in Fig. 9(a–f), where the melt pool depth/width ratio is greater than 1. Recoil pressure and surface tension are opposing forces acting perpendicularly to the melt pool surface. When a higher surface tension is used such as 2.5, 5, 7.5 and kg/s^2, the melt pool dynamic is governed by surface tension or in essence conduction and this melt pool regime is marked by the blue region in Fig. 10. In these cases, the surface tension is high, and the opposing recoil pressure due to evaporation is insufficient to create a vapor depression eventually leading to a shallower and wider melt pool. The melt pool morphology and thermo-fluid conditions for these surface tension dominant cases are visualized in Fig. 9(g–j), where the melt pool with depth/width ratio is less than 1. Wider melt pools are generally attributed to the Marangoni phenomenon in melt pool dynamics, but in this section this mechanism is ignored, as the surface tension is temperature independent and therefore surface tension is accountable for melt pool widening. The transition of the governing mechanism from recoil pressure to surface tension in the melt pool dynamics occurs between inverse Bond numbers of $1.6 \cdot 10^5$ and $5.4 \cdot 10^5$. By using linear interpolation, a threshold Bo^{-1} of $4 \cdot 10^5$ is calculated, which should theoretically form a melt pool with a depth/width ratio equal to 1 and hence the influence of recoil pressure and surface tension phenomena in the melt dynamics is theoretically equal. In real cases where surface tension varies with temperature i.e., when Marangoni convection is present, average surface tension can be used in Eq. (17), which can be calculated as the average surface tension between boiling and liquidus

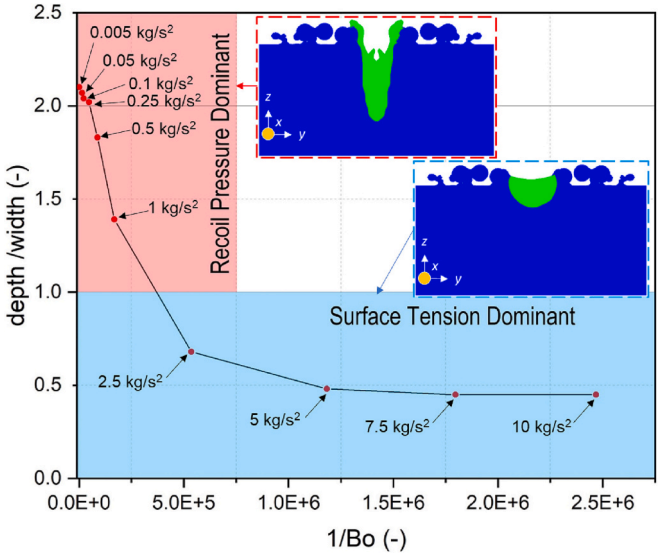

Fig. 10. Variation of melt pool depth to width ratio with the inverse of Bo. The recoil pressure and surface tension dominant zones are marked with red and blue color, along with the predicted melt pools from the extreme low surface tension 0.005 kg/s^2 (left) and highest surface tension 10 kg/s^2 (right) cases. (For interpretation of the references to color in this figure legend, the reader is referred to the web version of this article.)

temperatures. The change of surface tension in this liquid phase interval from 1733 K to 3200 K is −0.0008 kg/s^2/K as stated in Table 2. Therefore, a surface tension value of 0.2766 kg/s^2 which is a characteristic value for 316L stainless steel can be used in Eq. (17), to evaluate the dimensionless Bo number.

To correlate the resulting temperature field to surface tension, a plot of *Nu* (−) and average melt pool temperature against relative surface tension is shown in Fig. 11. The relative surface tension (σ_i/σ_T) is the ratio between σ_i, surface tension values used in this sensitivity study (0.005, 0.05, 0.1, 0.25, 0.5, 1, 2.5, 5, 7.5 and 10 kg/s^2) and the reference surface tension at liquidus temperature 1733 K for 316-L stainless steel, σ_T = 0.3282 kg/s^2. These material properties are also previously mentioned in Table 2.

From Fig. 11, it becomes clear that as the relative surface tension increases, the *Nu* decreases very rapidly and is only stabilized when the relative surface tension is equal to or greater than 2.5, where the melt pool is in the surface tension dominated conduction mode. *Nu* calculates the ratio of convective heat transfer to conductive heat transfer, hence with a decrease in *Nu* the dominant heat transfer mechanism changes from convection to conduction due to the increase in relative surface tension. An increase in relative surface tension above 2.5 does not affect *Nu,* and thus the heat transfer mechanism is still dominated by conduction and the change in the average melt pool temperature is also minimal. The change in the governing heat transfer mechanism with increasing surface tension was also noticed when comparing the melt pool shape and temperature gradient in Fig. 9, where the melt pool depth is reduced and heat is concentrated in a smaller molten pool. The increase in the average melt pool temperature is due to poor heat dissipation from the melt pool is displayed in Fig. 11. This proves that convection is highly efficient in heat dissipation, reducing the temperature gradient during the laser processing and therefore also lowering the residual stress. This can also have a direct effect on the melt pool microstructure, grain morphology and grain size as explained earlier [18]. Convection is a dominating heat transfer mechanism when recoil pressure is a governing force in the melt pool dynamics which can be confirmed by comparing Fig. 9, Figs. 10 and 11 at surface tension values below 2.5 kg/s^2. This implies that recoil pressure adds a higher linear momentum to the melt pool fluid flow, which efficiently reduces the average temperature.

The increase in the swelling of the back keyhole wall caused by humping for simulation cases with surface tension values between 0.005 and 1 kg/s^2 increases the temperature of the melt pool which is quantitatively shown in Fig. 11. The multiple reflection phenomenon inside the narrow keyhole increases the absorptivity and increases the temperature. This sensitivity study shows how the temperature and velocity fields are closely coupled to each other and also to the governing forces in the melt pool like recoil pressure and surface tension.

Reduced order models that ignore important phenomena like Marangoni convection and surface tension can lead to overestimation of melt pool temperatures as shown in Fig. 11, where the minimum fluid flow caused by using a high surface tension of 10 kg/s^2 predicts the highest melt pool temperature. In this case, the heat loss from the melt pool is almost solely based on conduction, which is a slower mechanism and hence heat accumulates in the melt pool. The temperature predictions of reduced order numerical models can be accurate only when a lower laser energy density is used for L-PBF processing either by selecting lower laser powers or faster scanning speeds. To reduce this error in prediction, the more fundamental work by Bayat et al. [49] included a calculation of an effective thermal conductivity derived from a high fidelity thermal-CFD numerical model. This updated material property can be used as an input to the reduced order model to compensate for the absent multi-physics and to predict accurate temperature fields. Therefore, computationally efficient reduced order models can be confidently used for predicting outcomes of L-PBF processes reducing time consumption.

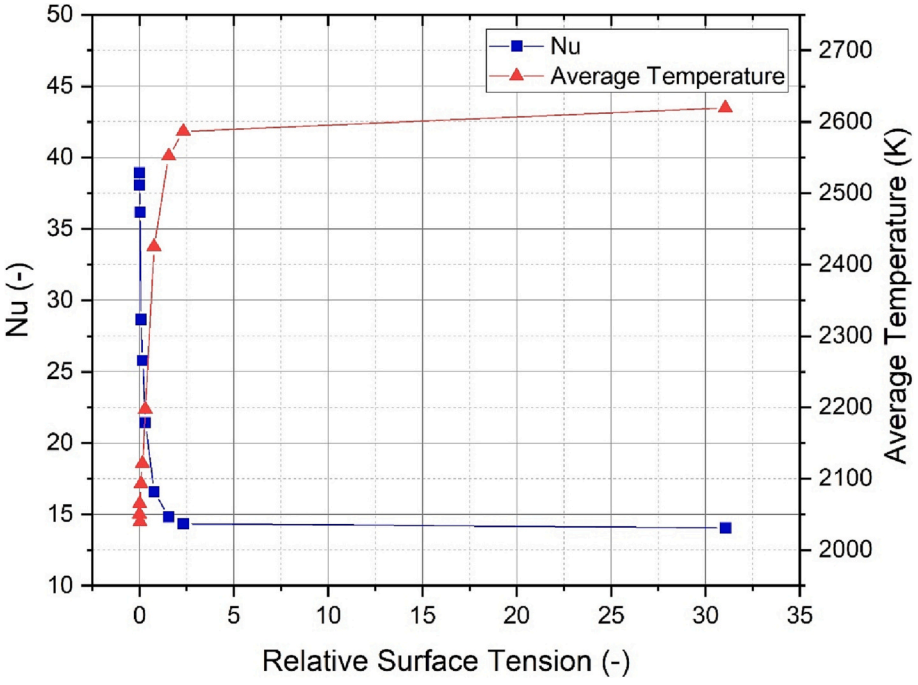

Fig. 11. Variation of *Nu* (–) and average melt pool temperature (K) with relative surface tension.

5. Conclusion

In this study, a meso-scale thermo-fluid numerical simulation using the FVM based software Flow-3D is presented for the L-PBF process of 316-L stainless steel. The numerical model is validated against single-track experiments, in which single laser tracks are printed on a substrate produced by a L-PBF. The predicted melt pool shape and dimensions match very well with the corresponding experimental results. Subsequently, two parametric studies are conducted to understand the role of recoil pressure as well as capillarity on the melt pool conditions.

In the recoil pressure sensitivity analysis, two sets of simulations are carried out for a range of LEDs and laser beam diameters, where the recoil pressure is set to be active and inactive, respectively. It is observed that the recoil pressure plays a minor role at LED values below 80 J/m for 20 μm beam size, below 160 J/m for 60 μm beam size, and below 280 J/m for a laser beam diameter of 120 μm. This underlines that with an increase in laser beam diameter the threshold LED value also increases.

In the surface tension parametric study, it is noted that the melt pool depth increases with an increase in the Bond number (*Bo*). This is because at lower Bo values, the melt pool dynamics will be dominated by surface tension and thus the impact of the opposing recoil pressure is eliminated. At high *Bo* numbers, the melt pool dynamic is dominated by the recoil pressure leading to bigger depressions and consequently larger melt pool depths. Varying the surface tension also significantly affects the heat transfer mode in the melt pool, where a low surface tension promotes convective heat transfer, whereas for a high surface tension conduction is dominant. For simulation cases where Bo^{-1} value is below $4{\cdot}10^5$, the recoil pressure is the controlling mechanism in the melt pool dynamics, whereas for values above $4{\cdot}10^5$ surface tension is dominant.

The results from the two parametric studies provide a process/material window elucidating which of the investigated mechanisms are important and which are not. Based on this, it can be determined when the high-fidelity multi-physics model can be replaced by a time efficient lower-fidelity reduced order model which ignores the non-significant physics. The future work will include validating the application of effective material properties in a low-fidelity, time-efficient reduced order model for a selected process window.

Declaration of competing interest

The authors have no conflicts of interest to declare.

Acknowledgment

This work has received funding from Independent Research Fund Denmark, the DIGI-3D project (contract no. 0136-00210B).

References

[1] Bayat M, Dong W, Thorborg J, To AC, Hattel JH. A review of multi-scale and multi-physics simulations of metal additive manufacturing processes with focus on modeling strategies. Addit Manuf 2021;47. https://doi.org/10.1016/j.addma.2021.102278.

[2] DebRoy T, Wei HL, Zuback JS, Mukherjee T, Elmer JW, Milewski JO, Beese AM, Wilson-Heid A, De A, Zhang W. Additive manufacturing of metallic components – process, structure and properties. Prog Mater Sci 2018;92:112–224. https://doi.org/10.1016/j.pmatsci.2017.10.001.

[3] DebRoy T, Mukherjee T, Milewski JO, Elmer JW, Ribic B, Blecher JJ, Zhang W. Scientific, technological and economic issues in metal printing and their solutions. Nat Mater 2019;18. https://doi.org/10.1038/s41563-019-0408-2.

[4] Weaver JS, Heigel JC, Lane BM. Laser spot size and scaling laws for laser beam additive manufacturing. J Manuf Process 2022;73:26–39. https://doi.org/10.1016/j.jmapro.2021.10.053.

[5] Metelkova J, Kinds Y, Kempen K, de Formanoir C, Witvrouw A, Van Hooreweder B. On the influence of laser defocusing in selective laser melting of 316L. Addit Manuf 2018;23:161–9. https://doi.org/10.1016/j.addma.2018.08.006.

[6] Raghavan N, Dehoff R, Pannala S, Simunovic S, Kirka M, Turner J, Carlson N, Babu SS. Numerical modeling of heat-transfer and the influence of process parameters on tailoring the grain morphology of IN718 in electron beam additive manufacturing *. Acta Mater 2016;112:303–14. https://doi.org/10.1016/j.actamat.2016.03.063.

[7] Bartlett JL, Li X. An overview of residual stresses in metal powder bed fusion. Addit Manuf 2019;27:131–49. https://doi.org/10.1016/j.addma.2019.02.020.

[8] Bajaj P, Hariharan A, Kini A, Kürnsteiner P, Raabe D, Jägle EA. Steels in additive manufacturing: a review of their microstructure and properties. Mater Sci Eng A 2020;772. https://doi.org/10.1016/j.msea.2019.138633.

[9] Ronneberg T, Davies CM, Hooper PA. Revealing relationships between porosity, microstructure and mechanical properties of laser powder bed fusion 316L stainless steel through heat treatment. Mater Des 2020;189:108481. https://doi.org/10.1016/j.matdes.2020.108481.

[10] Kruth JP, Levy G, Klocke F, Childs THC. Consolidation phenomena in laser and powder-bed based layered manufacturing. CIRP Ann Manuf Technol 2007;56:730–59. https://doi.org/10.1016/j.cirp.2007.10.004.

[11] Lane B, Zhirnov I, Mekhontsev S, Grantham S, Ricker R, Rauniyar S, Chou K. Transient laser energy absorption, co-axial melt pool monitoring, and relationship

to melt pool morphology. Addit Manuf 2020;36:101504. https://doi.org/10.1016/j.addma.2020.101504.
[12] McCann R, Obeidi MA, Hughes C, McCarthy É, Egan DS, Vijayaraghavan RK, Joshi AM, Acinas Garzon V, Dowling DP, McNally PJ, Brabazon D. In-situ sensing, process monitoring and machine control in laser powder bed fusion: a review. Addit Manuf 2021;45. https://doi.org/10.1016/j.addma.2021.102058.
[13] Imani F, Gaikwad A, Montazeri M, Rao P, Yang H, Reutzel E. Process mapping and in-process monitoring of porosity in laser powder bed fusion using layerwise optical imaging. J Manuf Sci Eng Trans ASME 2018;140. https://doi.org/10.1115/1.4040615.
[14] Bayat M, Mohanty S, Hattel JH. Multiphysics modelling of lack-of-fusion voids formation and evolution in IN718 made by multi-track/multi-layer L-PBF. Int J Heat Mass Transf 2019;139:95–114. https://doi.org/10.1016/j.ijheatmasstransfer.2019.05.003.
[15] Bayat M, Thanki A, Mohanty S, Witvrouw A, Yang S, Thorborg J, Tiedje NS, Hattel JH. Keyhole-induced porosities in laser-based powder bed fusion (L-PBF) of Ti6Al4V: high-fidelity modelling and experimental validation. Addit Manuf 2019;30. https://doi.org/10.1016/j.addma.2019.100835.
[16] Khairallah SA, Anderson AT, Rubenchik A, King WE. Laser powder-bed fusion additive manufacturing: physics of complex melt flow and formation mechanisms of pores, spatter, and denudation zones. Acta Mater 2016;108:36–45. https://doi.org/10.1016/j.actamat.2016.02.014.
[17] Le TN, Lo YL. Effects of sulfur concentration and Marangoni convection on melt-pool formation in transition mode of selective laser melting process. Mater Des 2019;179:107866. https://doi.org/10.1016/j.matdes.2019.107866.
[18] Mukherjee T, Wei HL, De A, DebRoy T. Heat and fluid flow in additive manufacturing – part II: powder bed fusion of stainless steel, and titanium, nickel and aluminum base alloys. Comput Mater Sci 2018;150:369–80. https://doi.org/10.1016/j.commatsci.2018.04.027.
[19] Mukherjee T, Wei HL, De A, DebRoy T. Heat and fluid flow in additive manufacturing—part I: modeling of powder bed fusion. Comput Mater Sci 2018;150:304–13. https://doi.org/10.1016/j.commatsci.2018.04.022.
[20] Wu YC, San CH, Chang CH, Lin HJ, Marwan R, Baba S, Hwang WS. Numerical modeling of melt-pool behavior in selective laser melting with random powder distribution and experimental validation. J Mater Process Technol 2018;254:72–8. https://doi.org/10.1016/j.jmatprotec.2017.11.032.
[21] Lee YS, Zhang W. Modeling of heat transfer, fluid flow and solidification microstructure of nickel-base superalloy fabricated by laser powder bed fusion. Addit Manuf 2016;12:178–88. https://doi.org/10.1016/j.addma.2016.05.003.
[22] Kim J, Lee S, Hong JK, Kang N, Choi YS. Calibration of laser penetration depth and absorptivity in finite element method based modeling of powder bed fusion melt pools. Met Mater Int 2020;26:891–902. https://doi.org/10.1007/s12540-019-00599-3.
[23] Shi Q, Gu D, Xia M, Cao S, Rong T. Effects of laser processing parameters on thermal behavior and melting/solidification mechanism during selective laser melting of TiC/Inconel 718 composites. Opt Laser Technol 2016;84:9–22. https://doi.org/10.1016/j.optlastec.2016.04.009.
[24] Criales LE, Arısoy YM, Özel T. Sensitivity analysis of material and process parameters in finite element modeling of selective laser melting of Inconel 625. Int J Adv Manuf Technol 2016;86:2653–66. https://doi.org/10.1007/s00170-015-8329-y.
[25] Foroozmehr A, Badrossamay M, Foroozmehr E, Golabi S. Finite element simulation of selective laser melting process considering optical penetration depth of laser in powder bed. Mater Des 2016;89:255–63. https://doi.org/10.1016/j.matdes.2015.10.002.
[26] Kamara AM, Marimuthu S, Li L. Finite element modeling of microstructure in laser-deposited multiple layer Inconel 718 parts. Mater Manuf Process 2014;29:1245–52. https://doi.org/10.1080/10426914.2014.930963.
[27] Vastola G, Pei QX, Zhang YW. Predictive model for porosity in powder-bed fusion additive manufacturing at high beam energy regime. Addit Manuf 2018;22:817–22. https://doi.org/10.1016/j.addma.2018.05.042.
[28] Mindt HW, Desmaison O, Megahed M. Modelling powder bed additive manufacturing defects. In: 7th Eur. Conf. Aeronaut. Sp. Sci. Model; 2015. p. 1–6.
[29] Shrestha S, Chou K. Mesoscopic simulation model to predict temperature distribution and melt pool size during selective laser scanning. In: ASME 2018 13th Int. Manuf. Sci. Eng. Conf., College Station, Texas, USA; 2018.
[30] Leitz KH, Grohs C, Singer P, Tabernig B, Plankensteiner A, Kestler H, Sigl LS. Fundamental analysis of the influence of powder characteristics in selective laser melting of molybdenum based on a multi-physical simulation model. Int J Refract Met Hard Mater 2018;72:1–8. https://doi.org/10.1016/j.ijrmhm.2017.11.034.
[31] Wang H, Zou Y. Microscale interaction between laser and metal powder in powder-bed additive manufacturing: conduction mode versus keyhole mode. Int J Heat Mass Transf 2019;142:118473. https://doi.org/10.1016/j.ijheatmasstransfer.2019.118473.
[32] Khairallah SA, Anderson A. Mesoscopic simulation model of selective laser melting of stainless steel powder. J Mater Process Technol 2014;214:2627–36. https://doi.org/10.1016/j.jmatprotec.2014.06.001.
[33] Tang C, Tan JL, Wong CH. A numerical investigation on the physical mechanisms of single track defects in selective laser melting. Int J Heat Mass Transf 2018;126:957–68. https://doi.org/10.1016/j.ijheatmasstransfer.2018.06.073.
[34] Tan W, Shin YC. Multi-scale modeling of solidification and microstructure development in laser keyhole welding process for austenitic stainless steel. Comput Mater Sci 2015;98:446–58. https://doi.org/10.1016/j.commatsci.2014.10.063.
[35] Lin R, Wang Hping, Lu F, Solomon J, Carlson BE. Numerical study of keyhole dynamics and keyhole-induced porosity formation in remote laser welding of Al alloys. Int. J. Heat Mass Transf. 2017;108:244–56. https://doi.org/10.1016/j.ijheatmasstransfer.2016.12.019.
[36] Panwisawas C, Perumal B, Ward RM, Turner N, Turner RP, Brooks JW, Basoalto HC. Keyhole formation and thermal fluid flow-induced porosity during laser fusion welding in titanium alloys: experimental and modelling. Acta Mater 2017;126:251–63. https://doi.org/10.1016/j.actamat.2016.12.062.
[37] Aggarwal A, Patel S, Kumar A. Selective laser melting of 316L stainless steel: physics of melting mode transition and its influence on microstructural and mechanical behavior. JOM 2019;71:1105–16. https://doi.org/10.1007/s11837-018-3271-8.
[38] Cook PS, Murphy AB. Simulation of melt pool behaviour during additive manufacturing: underlying physics and progress. Addit Manuf 2020;31:100909. https://doi.org/10.1016/j.addma.2019.100909.
[39] Mills KC, Keene BJ, Brooks RF, Shirlali A. In: Marangoni effects in welding; 1998. p. 911–25.
[40] Nan W, Ghadiri M. Numerical simulation of powder flow during spreading in additive manufacturing. Powder Technol 2019;342:801–7. https://doi.org/10.1016/j.powtec.2018.10.056.
[41] Wang L, Yu A, Li E, Shen H, Zhou Z. Effects of spreader geometry on powder spreading process in powder bed additive manufacturing. Powder Technol 2021;384:211–22. https://doi.org/10.1016/j.powtec.2021.02.022.
[42] Chen H, Chen Y, Liu Y, Wei Q, Shi Y, Yan W. Packing quality of powder layer during counter-rolling-type powder spreading process in additive manufacturing. Int J Mach Tool Manuf 2020;153:103553. https://doi.org/10.1016/j.ijmachtools.2020.103553.
[43] Lampitella V, Trofa M, Astarita A, D'Avino G. Discrete element method analysis of the spreading mechanism and its influence on powder bed characteristics in additive manufacturing. Micromachines 2021;12:392. https://doi.org/10.3390/mi12040392.
[44] Chen H, Wei Q, Zhang Y, Chen F, Shi Y, Yan W. Powder-spreading mechanisms in powder-bed-based additive manufacturing: experiments and computational modeling. Acta Mater 2019;179:158–71. https://doi.org/10.1016/j.actamat.2019.08.030.
[45] Mahmoodkhani Y, Ali U, Imani Shahabad S, Rani Kasinathan A, Esmaeilizadeh R, Keshavarzkermani A, Marzbanrad E, Toyserkani E. On the measurement of effective powder layer thickness in laser powder-bed fusion additive manufacturing of metals. Prog Addit Manuf 2019;4:109–16. https://doi.org/10.1007/s40964-018-0064-0.
[46] Körner C, Bauereiß A, Attar E. Fundamental consolidation mechanisms during selective beam melting of powders. Model Simul Mater Sci Eng 2013;21. https://doi.org/10.1088/0965-0393/21/8/085011.
[47] Bayat M, Mohanty S, Hattel JH. Multiphysics modelling of lack-of-fusion voids formation and evolution in IN718 made by multi-track/multi-layer L-PBF. Int J Heat Mass Transf 2019;139:95–114. https://doi.org/10.1016/j.ijheatmasstransfer.2019.05.003.
[48] Moshiri M, Loaldi D, Zanini F, Sgaravato D, Carmignato S, Tosello G. Analysis of an as-built metal additively manufactured tool cavity insert performance and advantages for plastic injection moulding. J Manuf Process 2021;61:369–82. https://doi.org/10.1016/j.jmapro.2020.11.035.
[49] Bayat M, Nadimpalli VK, Pedersen DB, Hattel JH. A fundamental investigation of thermo-capillarity in laser powder bed fusion of metals and alloys. Int J Heat Mass Transf 2021;166. https://doi.org/10.1016/j.ijheatmasstransfer.2020.120766.
[50] Chen H, Yan W. Spattering and denudation in laser powder bed fusion process: multiphase flow modelling. Acta Mater 2020;196:154–67. https://doi.org/10.1016/j.actamat.2020.06.033.
[51] Tang C, Le KQ, Wong CH. Physics of humping formation in laser powder bed fusion. Int J Heat Mass Transf 2020;149. https://doi.org/10.1016/j.ijheatmasstransfer.2019.119172.
[52] Bayat M, Mohanty S, Hattel JH. A systematic investigation of the effects of process parameters on heat and fluid flow and metallurgical conditions during laser-based powder bed fusion of Ti6Al4V alloy. Int J Heat Mass Transf 2019;139:213–30. https://doi.org/10.1016/j.ijheatmasstransfer.2019.05.017.